

Received July 5, 2018, accepted August 18, 2018, date of publication September 5, 2018, date of current version September 28, 2018.

Digital Object Identifier 10.1109/ACCESS.2018.2868724

# Reconfigurable K-Band MIMO Transmission With On-Board Vector Calibration

SEONG-MO MOON<sup>1</sup>, HAN LIM LEE<sup>2</sup>, (Member, IEEE), IN-BOK YOM<sup>1</sup>,  
AND MOON-QUE LEE<sup>3</sup>, (Member, IEEE)

<sup>1</sup>Satellite Technology Research Group, Electronics and Telecommunications Research Institute, Daejeon 34129, South Korea

<sup>2</sup>School of Electrical and Electronics Engineering, Chung-Ang University, Seoul 06974, South Korea

<sup>3</sup>School of Electrical Engineering and Computer Science, University of Seoul, Seoul 02504, South Korea

Corresponding author: Moon-Que Lee (mqlee@uos.ac.kr)

This work was supported by the Institute for Information & communications Technology Promotion through the Development of Core Technology for Satellite Payload, Korea Government (MSIT), under Grant 2018-0-00190.

**ABSTRACT** This paper presents a reconfigurable multi-input and multi-output amplifier architecture with on-board multiport vector calibration (MVC) for flexible multi-channel transmission in K-band. The proposed architecture controls phases of K-band transmission path to generate a diversity of source-to-target channel power assignment. In addition, the proposed calibration circuitry detects relative amplitude and phase of each transmission path and ensures high isolation at each output port. The proposed architecture consists of waveguide hybrid matrices, amplifier modules, including phase shifter, attenuator and 0°/180° phase inverter monolithic microwave integrated circuits (MMICs), and a MVC block. The MVC is configured with a modulator, two QPSK demodulator MMICs, a digital signal processing board, and 16 digital-to-analog converter units. For the verification of K-band applications, 4 × 4 multi-channel front end was implemented and showed reconfigurable performance as well as stable port-to-port isolation characteristics better than 26 dB from 19.5 to 22.5 GHz.

**INDEX TERMS** Multi-input and multi-output (MIMO), connected-vehicle, K-band transmission, MMIC, vector calibration.

## I. INTRODUCTION

With the convergence of vehicular applications and communication technologies, vehicle-to-everything (V2X) including vehicle-to-vehicle (V2V) and vehicle-to-infrastructure (V2I) is considered as the key requirement for the connected-vehicle of the future. Due to the potential ability of the connected-vehicles to provide a variety of services such as safety improvement, traffic control, data exchange, positioning, roadway information and autonomous driving, many researches have been conducted to prepare the emerging technology. Most of the researches have focused on the analysis of channel characteristics and adoption of IEEE 802.11p protocol [1]–[6]. However, since the number of sensors integrated into a vehicle expands and the rate of data they generate also increases, the 10-MHz channels in 5.9 GHz band will not be sufficient. That is, the future connected-vehicles will need gigabit per second (Gbps) data rate which can be achieved by the use of K/Ka-band. For the high bandwidth connected vehicles, many researches have already discussed about the use of mmWave communication on massive automotive

sensors, V2I scenarios, beamforming and vehicle positioning system [6]–[11]. Having K/Ka-band or mmWave as the viable solution to the connected vehicles, system operation flexibility and power allocation efficiency with multiple sensors and communication beams must also be increased. Since the frequency above K/Ka-band suffers from high propagation loss and susceptibility to blockage from other vehicles and buildings, and environmental conditions like rain drops, efficient transmission techniques must be investigated. Also, a vehicle needs to serve as an intermediate communication relay by sharing its sensing data through V2V to overcome the limited sensing range of a single vehicle. Thus, to support the simultaneous access to multiple devices and adjacent vehicles or infrastructures, flexible data and power distributions through multi-input and multi-outputs (MIMO) must be considered as well. Fig. 1 (a) shows the multi-channel connection within the concept of connected-vehicles including satellite communication. Fig. 1 (b) shows the typical multi-channel transmission through radio frequency (RF) power amplifiers (PA). Since each channel is designated to a fixed

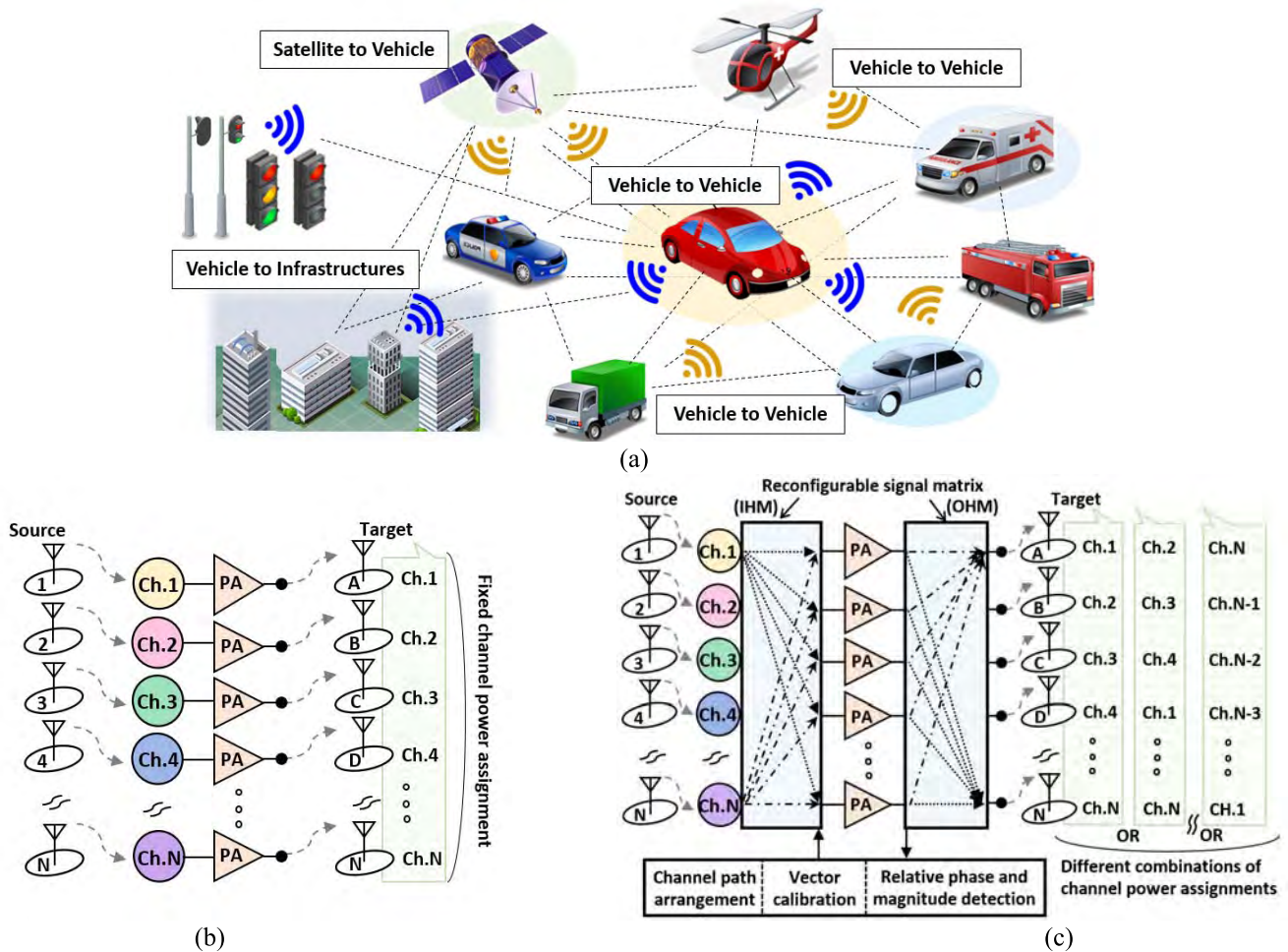


**FIGURE 1.** Simplified block diagrams of (a) the connected vehicle concept, (b) the conventional multi-channel power transmission and (c) reconfigurable multi-channel power transmission with automatic calibration.

target, flexible power distribution is not possible. Fig. 1 (c) shows the proposed architecture where each RF power amplifiers are shared with input hybrid matrix (IHM) and output hybrid matrix (OHM). The IHM distributes input signals and each distributed signal is amplified individually. Then, OHM recombines each signal and delivers each channel to different output ports. The fundamental operation is similar to the conventional multipoint amplifiers (MPA) [11] where each input is still generated to a fixed output port while flexible channel assignments can be possible in the proposed architecture. Although there have been a reconfigurable MPA using switchable input and output matrices [12], the implementation for K-band applications is difficult due to the requirement for accurate load impedance values in the matrices. Also, to deliver multi-channel signals from multiple sources to different targets, good isolation characteristics among the output ports should be achieved [13]. As shown in Fig. 1 (c), the proposed structure includes a vector calibration circuitry based on relative amplitude and phase detection.

Thus, in this paper, a new reconfigurable MIMO amplifier architecture with multipoint vector calibration (MVC) is

presented for multi-channel transmission. The proposed system is capable of distinguishing amplitude and phase errors in RF paths, and making optimized corrections for the corresponding errors to ensure high isolation among output channels. Also, the input-to-output power transmission paths can be flexibly controlled by adjusting the relative phase shifts of phase inverters whereas the conventional structure has fixed input-to-output signal paths.

## II. DESIGN OF RECONFIGURABLE MIMO SYSTEM

### A. OVERALL SYSTEM CONFIGURATION

Fig. 2 shows the block diagram of the proposed architecture with MVC for high output port-to-port isolation characteristics. The proposed reconfigurable system consists of an IHM, four linear phase shifters, four linear attenuators, four 0/180° phase inverters, four RF PAs, directional couplers, and an OHM. The directional couplers placed in front of the OHM take samples of each signal from the array paths and feed them to the MVC circuitry. The MVC consists of a quadrature phase-shift keying modulator, a power divider,

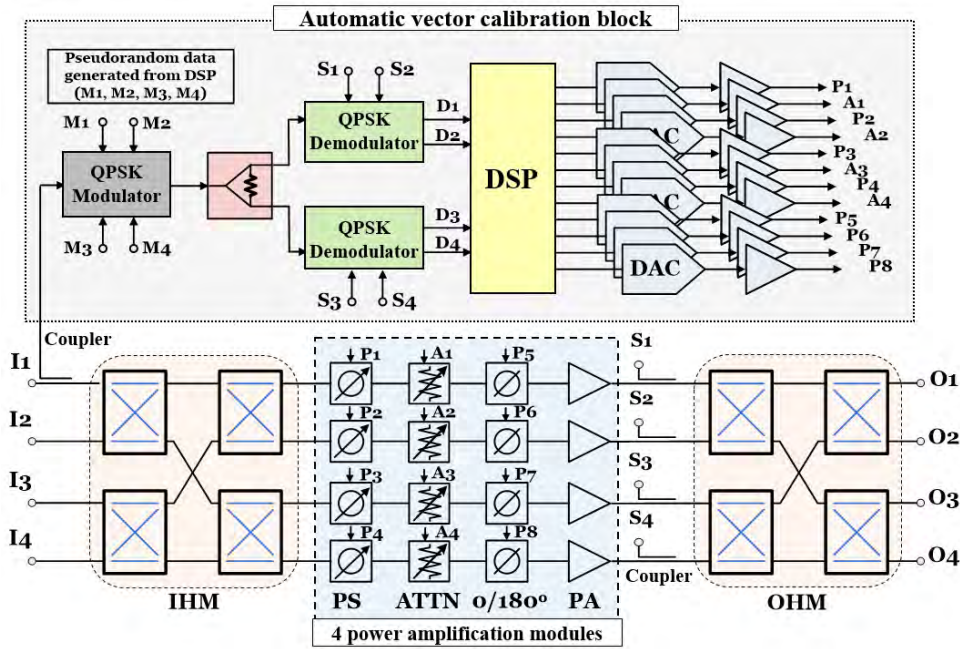


FIGURE 2. Block diagram of the proposed 4x4 system with the MVC circuitry.

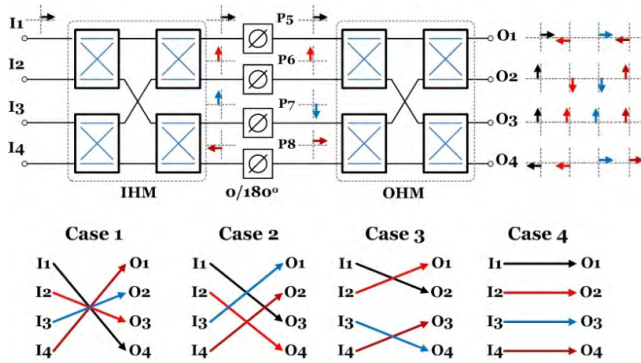


FIGURE 3. Reconfigurable input-to-output path selection of the proposed architecture.

two QPSK demodulators, a digital signal processing (DSP) board, and digital-to-analog converters (DAC). Amplitude and phase errors are detected and corrected through axial ratio calculations. More details on the calibration will be discussed later in this paper.

**B. FLEXIBLE OPERATION OF THE PROPOSED SYSTEM**

As mentioned previously, the multi-channel output pattern using the conventional MPA is fixed due to the passive implementation of IHM and OHM. They are usually implemented with four quadrature couplers as shown in Fig. 3 and thus the conventional MPA has the outputs ideally expressed as follows (case 1 in Fig.3).

$$O_1 = I_4 \cdot e^{-j\pi}; \quad O_2 = O_3 = O_4 = 0 \quad (1)$$

$$O_2 = I_3 \cdot e^{-j\pi}; \quad O_1 = O_3 = O_4 = 0 \quad (2)$$

$$O_3 = I_2 \cdot e^{-j\pi}; \quad O_1 = O_2 = O_4 = 0 \quad (3)$$

$$O_4 = I_1 \cdot e^{-j\pi}; \quad O_1 = O_2 = O_3 = 0 \quad (4)$$

However, as shown in Fig.3, phase shifters are added between the IHM and OHM to control the signal phases. Suppose the phase controlled by each phase shifter P5, P6, P7 and P8 are defined by  $\phi_1, \phi_2, \phi_3$  and  $\phi_4$ , respectively, the output signals can be expressed as follows.

$$O_1 = \frac{1}{4} \cdot \left[ I_1 \left( e^{-j\phi_1} + e^{-j(\phi_2+\pi)} + e^{-j(\phi_3+\pi)} + e^{-j\phi_4} \right) + I_2 \left( e^{-j(\phi_1+\pi/2)} + e^{-j(\phi_2+3\pi/2)} + e^{-j(\phi_3+\pi/2)} + e^{-j(\phi_4+3\pi/2)} \right) + I_3 \left( e^{-j(\phi_1+\pi/2)} + e^{-j(\phi_2+\pi/2)} + e^{-j(\phi_3+3\pi/2)} + e^{-j(\phi_4+3\pi/2)} \right) + I_4 \left( e^{-j(\phi_1+\pi)} + e^{-j(\phi_2+\pi)} + e^{-j(\phi_3+\pi)} + e^{-j(\phi_4+\pi)} \right) \right] \quad (5)$$

$$O_2 = \frac{1}{4} \cdot \left[ I_1 \left( e^{-j(\phi_1+\pi/2)} + e^{-j(\phi_2+3\pi/2)} + e^{-j(\phi_3+\pi/2)} + e^{-j(\phi_4+3\pi/2)} \right) + I_2 \left( e^{-j(\phi_1+\pi)} + e^{-j\phi_2} + e^{-j\phi_3} + e^{-j(\phi_4+\pi)} \right) + I_3 \left( e^{-j(\phi_1+\pi)} + e^{-j(\phi_2+\pi)} + e^{-j(\phi_3+\pi)} + e^{-j(\phi_4+\pi)} \right) + I_4 \left( e^{-j(\phi_1+3\pi/2)} + e^{-j(\phi_2+3\pi/2)} + e^{-j(\phi_3+\pi/2)} + e^{-j(\phi_4+\pi/2)} \right) \right] \quad (6)$$

$$O_3 = \frac{1}{4} \cdot \left[ I_1 \left( e^{-j(\phi_1+\pi/2)} + e^{-j(\phi_2+\pi/2)} + e^{-j(\phi_3+3\pi/2)} \right) \right]$$

$$\begin{aligned}
 &+ e^{-j(\phi_4+3\pi/2)}) \\
 &+ I_2 \left( e^{-j(\phi_1+\pi)} + e^{-j(\phi_2+\pi)} + e^{-j(\phi_3+\pi)} + e^{-j(\phi_4+\pi)} \right) \\
 &+ I_3 \left( e^{-j(\phi_1+\pi)} + e^{-j\phi_2} + e^{-j\phi_3} + e^{-j(\phi_4+\pi)} \right) \\
 &+ I_4 \left( e^{-j(\phi_1+3\pi/2)} + e^{-j(\phi_2+3\pi/2)} + e^{-j(\phi_3+3\pi/2)} \right. \\
 &\left. + e^{-j(\phi_4+3\pi/2)} \right) \tag{7}
 \end{aligned}$$

$$\begin{aligned}
 O_4 &= \frac{1}{4} \cdot \left[ I_1 \left( e^{-j(\phi_1+\pi)} + e^{-j(\phi_2+\pi)} + e^{-j(\phi_3+\pi)} + e^{-j(\phi_4+\pi)} \right) \right. \\
 &+ I_2 \left( e^{-j(\phi_1+3\pi/2)} + e^{-j(\phi_2+3\pi/2)} + e^{-j(\phi_3+\pi/2)} + e^{-j(\phi_4+\pi/2)} \right) \\
 &+ I_3 \left( e^{-j(\phi_1+3\pi/2)} + e^{-j(\phi_2+\pi/2)} + e^{-j(\phi_3+3\pi/2)} + e^{-j(\phi_4+\pi/2)} \right) \\
 &\left. + I_4 \left( e^{-j\phi_1} + e^{-j(\phi_2+\pi)} + e^{-j(\phi_3+\pi)} + e^{-j\phi_4} \right) \right] \tag{8}
 \end{aligned}$$

According to (5)-(8), if each  $\phi$  is set to 0, then the output configuration becomes exactly same as the conventional MPA. However, if each  $\phi$  can be controlled by 0 and  $\pi$ , the input-to-output signal paths can be varied. For example, if we make  $\phi_1 = 0, \phi_2 = 0, \phi_3 = \pi$  and  $\phi_4 = \pi$ , then the input-to-output signal path will be like case 2 in Fig.3. Similarly,  $\phi_1 = 0, \phi_2 = \pi, \phi_3 = 0$  and  $\phi_4 = \pi$  will correspond to case 3 while  $\phi_1 = 0, \phi_2 = \pi, \phi_3 = \pi$  and  $\phi_4 = 0$  will be like case 4 in Fig.3. Therefore, 0/180° phase inverters are added in the proposed flexible system structure to overcome the fixed signal flow in the conventional structure. Table 1 summarizes the required phase set-up for the phase shifters P<sub>5</sub> to P<sub>8</sub> to make a variety of input-to-output pattern corresponding to Fig.3.

### III. DESIGN OF MULTI-PORT VECTOR CALIBRATION

Since exact combinations of phase and amplitude are required for the proposed system to work optimally, any imbalance in the amplitude and phase for each signal path should be adjusted. This correction can be achieved through proper manipulations of the linear phase shifters and attenuators. That is, a proper calibration scheme which can automatically adjust the phase and amplitude balance is required for high port-to-port isolation characteristics. The proposed calibration block consists of a QPSK modulator, two QPSK demodulators, a DSP block with DACs to control the attenuators and phase shifters as shown in Fig. 2.

#### A. DEMODULATOR MODULE

Fig. 4 shows the structure of the QPSK demodulator with two binary phase-shift keying (BPSK) demodulators, a power divider, phase shifters and attenuators for optimized amplitude and phase detections. Here, the phase shifters and attenuators are used to prevent any additional amplitude and phase errors from being added to desired MPA path imbalances. Fig. 5 shows the BPSK demodulator

MMIC that is fabricated in 0.15- $\mu$ m GaAs pHEMT process. At each output port of the BPSK demodulator, a diode detector is integrated to detect an in-phase signal and

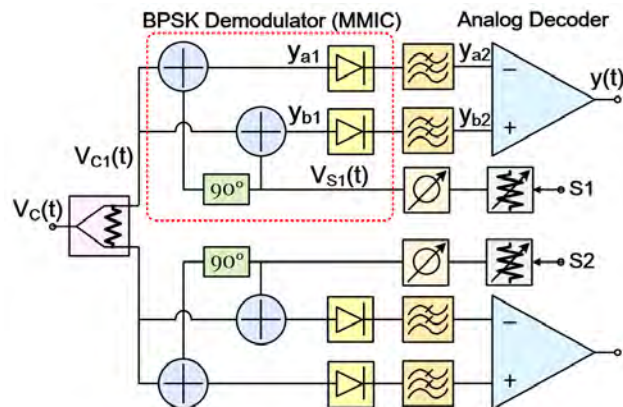


FIGURE 4. Structure of the QPSK demodulator using two BPSK demodulators combined together with additional phase shifters and attenuators.

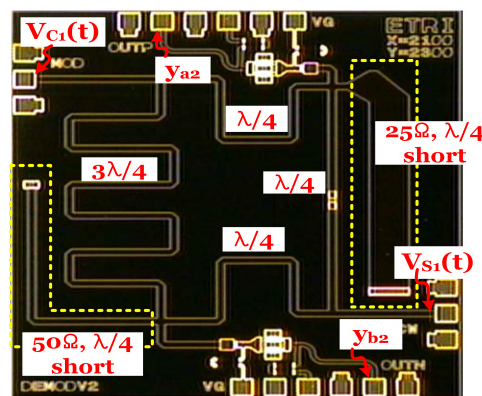
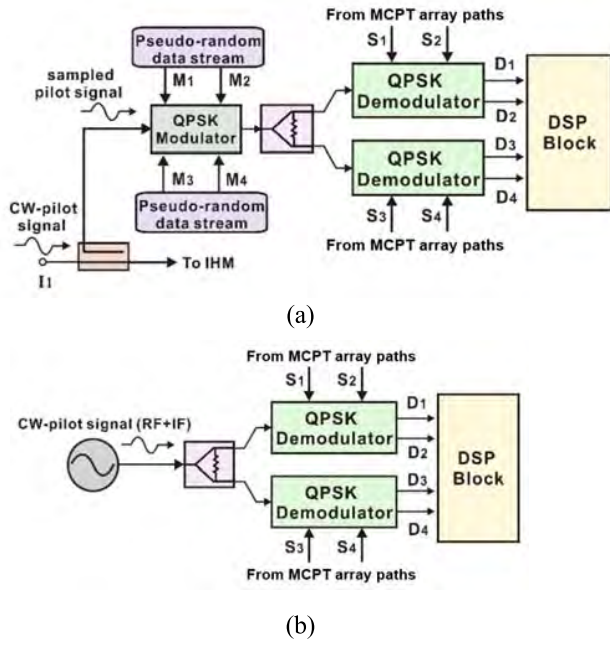


FIGURE 5. Fabricated BPSK demodulator using a wideband rat-race coupler.

out-of-phase signal which are the sum and the difference between the input and LO signals, respectively. The required I/Q signals of the LO ports are the quadrature signals coupled by directional couplers from each RF array path. Two BPSK demodulators can be configured into a single QPSK demodulator. If four sampled signals are needed to calibrate four RF signals, a dual-QPSK demodulator with analog decoder can be used.

The fundamental operation of the MVC block configured by QPSK modulator and demodulators can be described by Fig. 6. Fig. 6 (a) shows the proposed MVC structure configured with a QPSK modulator and a dual-QPSK demodulator. First, a continuous wave (CW) pilot signal is inserted into one of four inputs for calibration purpose. The CW-pilot signal is coupled by the directional coupler and the sampled signal is fed to the QPSK modulator. The CW-pilot signal gets modulated by the QPSK modulator with pseudo-random data at 10 Mbps which is to be the low-IF signal in a DSP block. Then, the QPSK-modulated CW-pilot signal is injected to the RF port of the dual-QPSK demodulator through Wilkinson power divider. After that, the modulated CW-pilot signal is demodulated with S<sub>1</sub>, S<sub>2</sub>, S<sub>3</sub>, and S<sub>4</sub> signals sampled from



**FIGURE 6.** The proposed MVC block by (a) QPSK modulator with data rate at 10 Mbps and (b) signal generator with pilot signal at a frequency of RF+10MHz.

the MPA array paths as shown in Fig. 2. The CW-pilot signal is at the same frequency as the  $S_1$ ,  $S_2$ ,  $S_3$ , and  $S_4$  signals and thus the demodulated signals ( $D_1$ ,  $D_2$ ,  $D_3$ , and  $D_4$ ) are down-converted into low-IF signals of 10 MHz. Since the down-converted IF signals include the phase and amplitude errors occurred at the RF paths of the proposed structure, the imbalances among the paths can be accurately analyzed through DSP and corrected by adjusting the attenuators and phase shifters of the corresponding paths. For numerical analysis, the case1 from Table 1 is assumed. If  $I_1$  is used as the input port for the calibration as shown in Fig. 2, the ideal amplitudes at  $S_1$ ,  $S_2$ ,  $S_3$ , and  $S_4$  should be equal and their ideal phases should be  $0^\circ$ ,  $90^\circ$ ,  $90^\circ$ , and  $180^\circ$ , respectively. Having the signal sampled from  $I_1$  after the QPSK modulator and the signals sampled after PAs denoted as  $V_{mod}$  and  $V_{CW}$ , respectively, the following equations can be derived.

$$v_{mod} = A_{mod} \cos(\omega_{mod} t + \phi_{mod}) \quad (9)$$

$$v_{CW} = A_{CW} \cos(\omega_{CW} t + \varphi_{Si}) \quad (10)$$

Here,  $\varphi_{Si}$  represents the CW phases of  $0^\circ$ ,  $90^\circ$ ,  $90^\circ$ , and  $180^\circ$  with respect to  $i = 1, 2, 3$ , and  $4$ , respectively. Then, (9) and (10) are injected into the BPSK demodulator where LO frequency is synchronized with the RF carrier ( $\omega_{mod} = \omega_{CW}$ ). The outputs of the detectors,  $y_{a2}$  and  $y_{b2}$ , for the case of  $\varphi_{Si} = 0^\circ$  (i.e.  $S_1$ ) can be determined by

$$y_{a2} = L \left[ \{A_{mod} \cos(\omega_{mod} t + \varphi_{mod}) + A_{CW} \cos(\omega_{CW} t)\}^2 \right] \\ = \frac{1}{2} (A_{mod}^2 + A_{CW}^2) + A_{mod} A_{CW} \cos(\varphi_{mod}) \quad (11)$$

**TABLE 1.** Summary of the required phases by the phase inverters corresponding to the operation cases in Figure 3.

	Case1	Case2	Case3	Case4
$P_5$ phase	$0^\circ$	$0^\circ$	$0^\circ$	$0^\circ$
$P_6$ phase	$0^\circ$	$0^\circ$	$180^\circ$	$180^\circ$
$P_7$ phase	$0^\circ$	$180^\circ$	$0^\circ$	$180^\circ$
$P_8$ phase	$0^\circ$	$180^\circ$	$180^\circ$	$0^\circ$

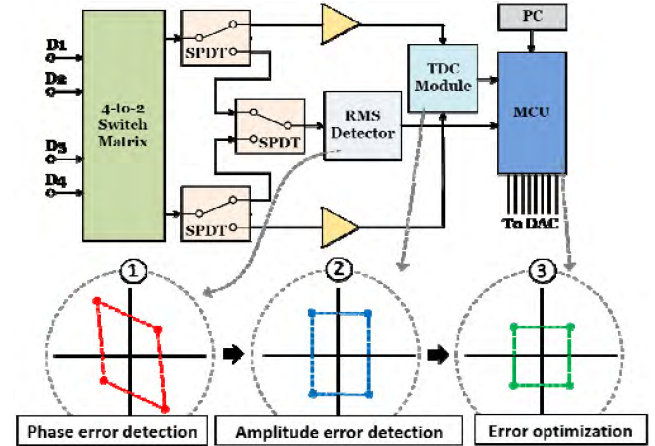


**FIGURE 7.** Block diagram and processing procedure of the digital part in the proposed automatic calibration circuitry.

$$y_{b2} = L \left[ \{A_{mod} \cos(\omega_{mod} t + \varphi_{mod}) - A_{CW} \cos(\omega_{CW} t)\}^2 \right] \\ = \frac{1}{2} (A_{mod}^2 + A_{CW}^2) - A_{mod} A_{CW} \cos(\varphi_{mod}). \quad (12)$$

In the above equations,  $L[\bullet]$  denotes the low-pass filtering for the parameter in the square bracket. Subtracting the outputs of the detectors ( $y_{b2} - y_{a2}$ ), the analog decoder output,  $y(t)$ , can be found as

$$y(t) = 2A_{mod} A_{CW} \cos(\varphi_{mod}). \quad (13)$$

It is noted that DC offsets are eliminated during the subtraction. Similarly for the case of  $\varphi_{Si} = 90^\circ$  (i.e.  $S_2$  or  $S_3$ ), the final output becomes

$$y(t) = 2A_{mod} A_{CW} \sin(\varphi_{mod}). \quad (14)$$

Lastly for the case of  $\varphi_{Si} = 180^\circ$ , the final output becomes

$$y(t) = -2A_{mod} A_{CW} \cos(\varphi_{mod}). \quad (15)$$

Thus, one QPSK demodulator can successfully demodulate I-data by (13) and Q-data by (14). Similarly, the other QPSK demodulator can successfully demodulate Q-data by (14) and inverted I-data by (15) for the  $4 \times 4$  system. However, a signal generator is used instead of the QPSK modulator as shown in Fig. 10 (b) for the ease of verification in this paper. The fundamental operation remains the same since the signal generator provides the frequency of RF+IF which is demodulated by LO (=RF) and consequently down-converted to IF (=10 MHz). Then, the down-converted signals ( $D_1$ ,  $D_2$ ,  $D_3$ , and  $D_4$ ) are analyzed by DSP to control the phase shifters and attenuators.

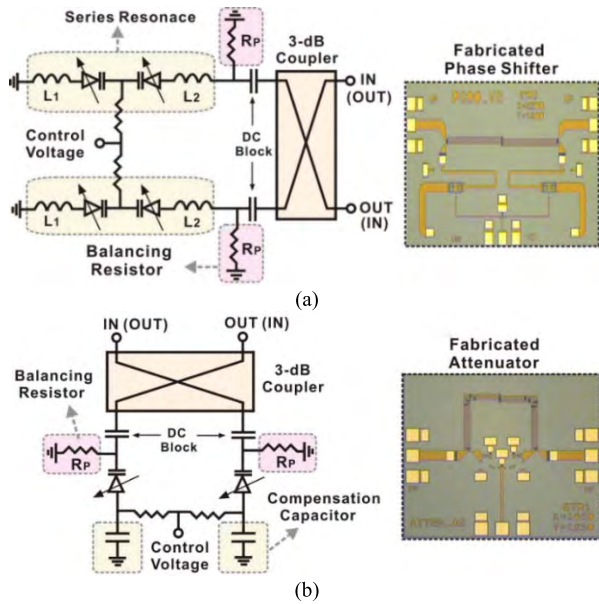


**FIGURE 8.** Implementation of the (a) phase shifter and (b) attenuator MMICs.

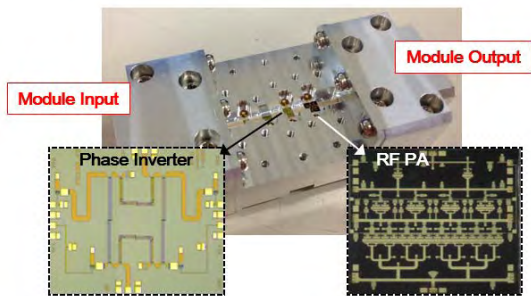
## B. DIGITAL SIGNAL PROCESSING FOR CALIBRATION

Fig. 7 describes the DSP part of the proposed MVC block with a processing step. The DSP block consists of a 4-to-2 switch matrix, three SPDT switches, an RMS detector, a time-to-digital converter (TDC) module, and a micro-controller unit (MCU). To find the relative phase imbalance among the down-converted signals, phase comparisons are first conducted by measuring the delays in rising times of two signals through the TDC module. Then, amplitude comparisons are conducted by measuring magnitude levels through the RMS detector. Using the measured phase and amplitude data, the MCU adjusts control-voltages for the phase shifters and attenuators through DACs.

## IV. IMPLEMENTATION AND MEASUREMENT

### A. POWER AMPLIFIER MODULE

As shown in Fig. 2, each power amplification (PA) module is configured with a voltage-controlled linear attenuator, a voltage-controlled linear phase shifter [14], a 0/180° phase inverter [15], and a PA. The attenuators and phase shifters in the amplification module were designed as MMICs and fabricated in 0.15- $\mu\text{m}$  GaAs pHEMT process. The voltage-controlled attenuator and phase shifter were both reflection types using Lange couplers for wideband operation as shown in Fig. 8. For the attenuator MMIC, a compact folded Lange coupler was adopted and a Schottky diode with forward bias was used as a variable resistor. Also, capacitors were added in-series with the Schottky diodes to compensate the phase variations occurred when reflective load impedances change. By adjusting the control voltage from 0.5 to 2.0 V, the maximum measured attenuation was about 7 dB with phase variation less than 3°. The measured input and output return losses were better than 13 dB from 15 to 25 GHz. Similarly,



**FIGURE 9.** Implemented power amplifier module.

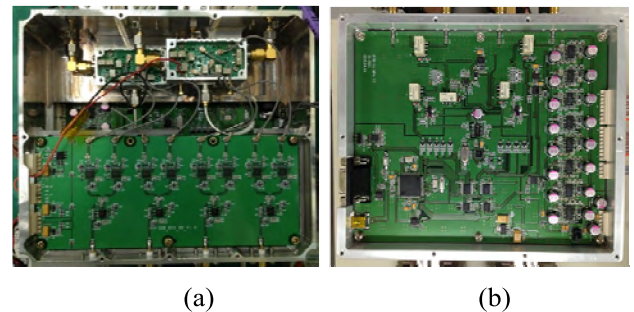


**FIGURE 10.** Implemented (a) 4x4 demodulator module and (b) DSP module.

the voltage-controlled linear phase shifter had measured maximum phase shift of 104° with insertion loss variation less than 0.2 dB from 17 to 25 GHz. Also, the phase inverter had measured phase shift of  $179 \pm 1.5^\circ$  from 17.5 to 22.5 GHz. The design details on the phase shifter and phase inverter are well-described in [14] and [15]. For PA, the measured saturation power,  $P_1$ -dB, and gain were 21 dBm and 17 dB, respectively at 21 GHz. The input and output return losses were better than 15 dB and 20 dB, respectively, from 18 to 30 GHz. Fig. 9 shows the complete amplification module consisting of an attenuator, a phase shifter, a phase inverter and an RF PA. The implemented PA module showed the measured gain of 8 dB with linear attenuation and phase shift ranges up to 7 dB and 100°, respectively. Also, the input and output return losses of the amplifier module were all better than 12 dB from 19.5 to 22.5 GHz.

### B. MULTIPOINT VECTOR CALIBRATION

Fig. 10 (a) and (b) shows the implementation of the 4 $\times$ 4 demodulator and DAC integrated DSP block. For sampling the RF signals, a directional coupler with a 12 dB coupling factor was used for each transmission array path. For the DSP block, the 4-to-2 switch matrix was configured with six AGN200A4H relay switches and LM3S9B92 micro-controller was used. Also, DAC was implemented using sixteen AD5628 chips. Fig. 11 shows the measurement set-up and implementation of the proposed 4 $\times$ 4 mmWave system with the MVC hardware. First, the DSP-based calibration flow was conducted with two demodulated signals taken

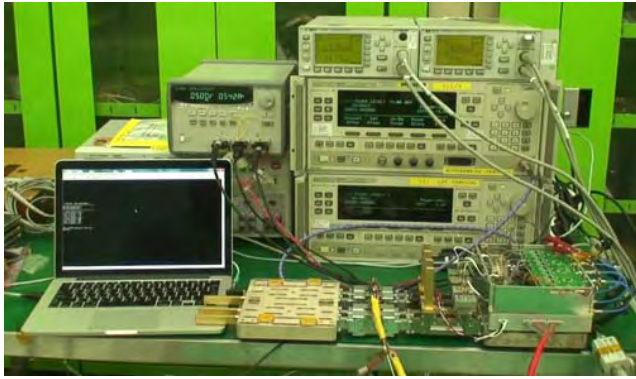


FIGURE 11. Measurement set-up and the complete reconfigurable multi-channel system with MVC.

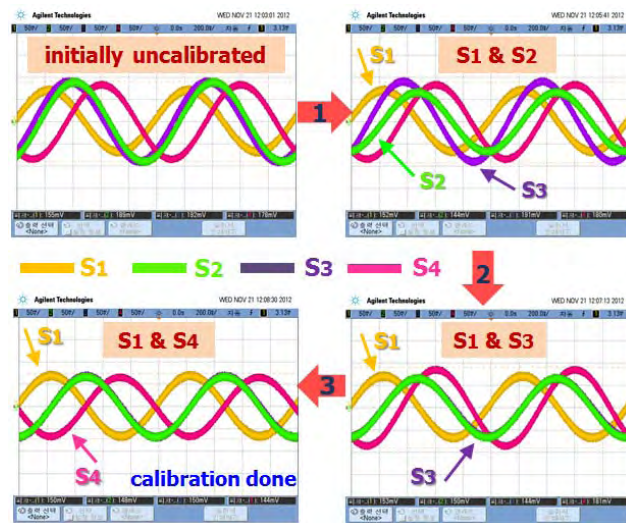


FIGURE 12. Sequential calibration results based on step-by-step comparison.

into account. Since there were four demodulated signals, one is taken as a reference for the comparison with the other three signals. Thus, a total of three calibration steps were needed and can be described as follows. Having  $D_1$  (referring to Fig. 7) as a reference, the first phase and amplitude comparisons between  $D_1$  and  $D_2$  by the TDC module and RMS detector were conducted. Based on the comparison result, the MCU connected with DAC controlled the phase shifter and attenuator in the corresponding path to correct the phase and amplitude deviations. Similarly, the rest of path errors were corrected by the comparisons between  $D_1$  and  $D_3$ , and between  $D_1$  and  $D_4$ , sequentially. The sequential calibration results corresponding to each correction step are shown in Fig. 12. Then, S-parameters of the proposed  $4 \times 4$  system were measured after the MVC was conducted at 21 GHz. Fig. 13 shows the port-to-port isolation characteristics over frequency when CW-pilot signal was injected into  $I_1$  as denoted in Fig. 2. The whole calibration was completed within 10 seconds. The measured return losses for all ports were better than 25 dB over the frequency range

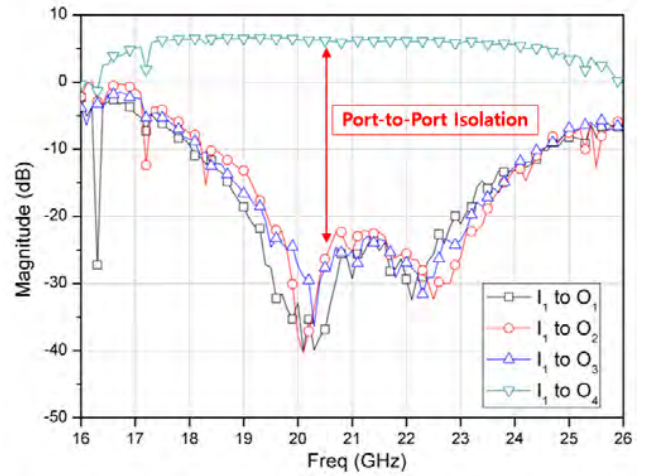


FIGURE 13. Measured S-parameters of the proposed  $4 \times 4$  MPA after calibration.

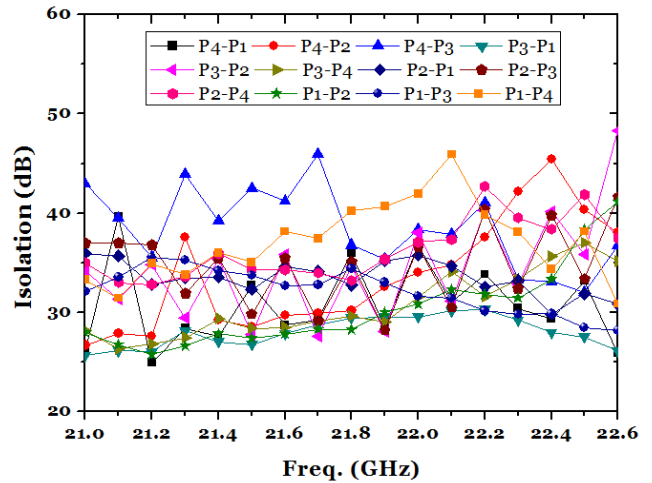


FIGURE 14. Measured isolation characteristics after calibration.

TABLE 2. Measured selective output power and isolation by using  $I_1$  and  $I_3$ .

		@ 19.5GHz	$O_1$	$O_2$	$O_3$	$O_4$
$I_1$	Power (dBm)		-28.5	-22.3	-18.6	9.8
	Isolation (dB)		38.3	32.1	28.4	-
$I_3$	Power (dBm)		-19.5	10.1	-18.8	-20.8
	Isolation (dB)		29.6	-	28.9	30.9

between 19.5 and 22.5 GHz. The measured output port-to-port isolation was always better than 26 dB in the operation band while the maximum measured isolation was about 50 dB. That is, the proposed MVC process, which needs only three sequential steps, does not require multiple numbers of redundant calibration iterations over every frequency in the operation band to get good isolation characteristics. Finally, Fig. 14 shows the completed isolation characteristics among the whole system ports. Also, for the output power characteristics of the proposed system, input power of 3 dBm

was injected to  $I_1$  and  $I_3$  separately at 19.5 GHz and the measured results are summarized in Table 2.

## V. CONCLUSION

In this paper, reconfigurable  $4 \times 4$  multi-channel MIMO transmission system with MVC was proposed and verified. The designed system showed excellent port-to-port isolation characteristics of always better than 26 dB from 19.5 to 22.5 GHz through a single calibration process. The proposed MVC block was able to detect and calibrate the amplitude and phase errors in the array paths by manipulating sampled signals with a straightforward and simple calibration process. Therefore, the proposed system including calibration was validated as an efficient solution to K-band transmission systems for connected vehicles and expected to be a promising technique for mmWave applications as well.

## REFERENCES

- [1] P. Liu, B. Ai, D. W. Matolak, R. Sun, and Y. Li, "5-GHz vehicle-to-vehicle channel characterization for example overpass channels," *IEEE Trans. Veh. Technol.*, vol. 65, no. 8, pp. 5862–5873, Aug. 2016.
- [2] P. Belanovic, D. Valerio, A. Paier, T. Zemen, F. Ricciato, and C. F. Mecklenbrauker, "On Wireless Links for Vehicle-to-Infrastructure Communications," *IEEE Trans. Veh. Technol.*, vol. 59, no. 1, pp. 269–282, Jan. 2010.
- [3] J. A. Fernandez, K. Borries, L. Cheng, B. V. K. V. Kumar, D. D. Stancil, and F. Bai, "Performance of the 802.11p physical layer in vehicle-to-vehicle environments," *IEEE Trans. Veh. Technol.*, vol. 61, no. 1, pp. 3–14, Jan. 2012.
- [4] E. Belyaev, A. Vinel, A. Surak, M. Gabbouj, M. Jonsson, and K. Egiuzarian, "Robust vehicle-to-infrastructure video transmission for road surveillance applications," *IEEE Trans. Veh. Technol.*, vol. 64, no. 7, pp. 2991–3003, Jul. 2015.
- [5] R. He et al., "Vehicle-to-Vehicle radio channel characterization in cross-road scenarios," *IEEE Trans. Veh. Technol.*, vol. 65, no. 8, pp. 5850–5861, Aug. 2016.
- [6] N. Lu, N. Cheng, N. Zhang, X. Shen, and J. W. Mark, "Connected vehicles: Solutions and challenges," *IEEE Internet Things J.*, vol. 1, no. 4, pp. 289–299, Aug. 2014.
- [7] J. Choi, V. Va, N. Gonzalez-Prelcic, R. Daniels, C. R. Bhat, and R. W. Heath, Jr., "Millimeter-wave vehicular communication to support massive automotive sensing," *IEEE Commun. Mag.*, vol. 54, no. 12, pp. 160–167, Dec. 2016.
- [8] L. Kong, M. K. Khan, F. Wu, G. Chen, and P. Zeng, "Millimeter-wave wireless communications for IoT-cloud supported autonomous vehicles: Overview, design, and challenges," *IEEE Commun. Mag.*, vol. 55, no. 1, pp. 62–68, Jan. 2017.
- [9] V. Va, T. Shimizu, G. Bansal, and R. W. Heath, Jr., "Beam design for beam switching based millimeter wave vehicle-to-infrastructure communications," in *Proc. ICC*, May 2016, pp. 1–6.
- [10] X. Cui, T. A. Gulliver, J. Li, and H. Zhang, "Vehicle positioning using 5G millimeter-wave systems," *IEEE Access*, vol. 4, pp. 6964–6973, Oct. 2016.
- [11] A. Mallet, A. Anakabe, J. Sombrin, and R. Rodriguez, "Multiport-amplifier-based architecture versus classical architecture for space telecommunication payloads," *IEEE Trans. Microw. Theory Techn.*, vol. 54, no. 12, pp. 4353–4361, Dec. 2006.
- [12] H. L. Lee, M.-Q. Lee, and J.-W. Yu, "Reconfigurable  $4 \times 4$  multi-port amplifier with switchable input and output matrices," *IET Microw. Antennas Propag.*, vol. 10, no. 12, pp. 1312–1321, 2016.
- [13] H. L. Lee, M.-Q. Lee, and J.-W. Yu, "Analysis of multi-port amplifier calibration for optimal magnitude and phase error detection," *IET Microw. Antennas Propag.*, vol. 10, no. 1, pp. 102–110, 2016.
- [14] H. L. Lee, S.-M. Moon, M.-Q. Lee, and J.-W. Yu, "Design of compact broadband phase shifter with constant loss variation," *Microw. Opt. Techn. Lett.*, vol. 56, no. 2, pp. 394–400, Feb. 2014.
- [15] H. L. Lee, S.-M. Moon, H.-J. Dong, M.-Q. Lee, and J.-W. Yu, "K-band  $0/180^\circ$  balanced phase shifter with dc-offset cancellation," *Electron. Lett.*, vol. 49, no. 19, pp. 1234–1235, Sep. 2013.



**SEONG-MO MOON** received the B.S., M.S., and Ph.D. degrees in electrical engineering from the University of Seoul, Seoul, South Korea, in 2003, 2005, and 2010, respectively. From 2005 to 2008, he was a Senior Research Engineer with Analog Devices, Inc., Seongnam, South Korea, where he was involved in RFIC design, such as voltage-controlled oscillator and local oscillator generation blocks. He is currently a Senior Engineer with the Electronics and Telecommunications Research Institute, Daejeon, South Korea, where he is involved in the development of RF and digital modules and systems for next-generation satellite payload. His research interests are analysis of nonlinearities of microwave active components, such as amplifier, and oscillator, and design of RFICs and monolithic microwave integrated circuits based on silicon, gallium arsenide, and gallium nitride for satellite payloads.



**HAN LIM LEE** received the B.A.Sc. degree from Simon Fraser University, Burnaby, BC, Canada, in 2008, and the M.S. and Ph.D. degrees in electrical engineering from Korea Advanced Institute of Technology, Daejeon, South Korea, in 2010 and 2014, respectively. From 2014 to 2015, he was with Samsung Electronics DMC R&D Center. Since 2015, he has been an Assistant Professor with the School of Electrical and Electronics Engineering, Chung-Ang University, Seoul, South Korea. His research interests include RF/microwave circuits, RF system applications, RFIC/monolithic microwave integrated circuit, and antenna design.



**IN-BOK YOM** received the B.S. degree from Hanyang University in 1990 and the M.S. and Ph.D. degrees from Chungnam National University, Daejeon, South Korea, in 2004 and 2007, respectively. Since 1990, he has been a Principal Research Member and the Managing Director of the Satellite Technology Research Group, Electronics and Telecommunications Research Institute. His research interests include microwave component, phased array antenna, and satellite system engineering.



**MOON-QUE LEE** received the B.S. degree in electrical engineering from the Korea Advanced Institute of Technology, Daejeon, South Korea, in 1992, and the M.S. and Ph.D. degrees in electrical engineering from Seoul National University, Seoul, South Korea, in 1994 and 1999, respectively. From 1999 to 2002, he was a Research Engineer with the Electronics and Telecommunications Research Institute. Since 2002, he has been a Professor of electrical engineering with the University of Seoul, Seoul. Since 2015, he has been a Creative Planner for Radio & Satellite with the the Ministry of Science, ICT and Future Planning, Korea Government. He is the author of over 53 international journals, 17 domestic/international patents, and nine RF and Microwave engineering books. His research interests emphasize microwave/millimeter-wave circuits monolithic microwave integrated circuits and hybrid circuits, wireless communication, and radar systems. He was a recipient of the 7th IEEE international conference on RFID Best Paper Award in 2013.